

Layered SnS sodium ion battery anodes synthesized near room temperature

Chuan Xia, Fan Zhang, Hanfeng Liang, and Husam N. Alshareef (✉)

Materials Science and Engineering, King Abdullah University of Science and Technology (KAUST), Thuwal 23955-6900, Saudi Arabia

Received: 22 April 2017

Revised: 10 June 2017

Accepted: 11 June 2017

© Tsinghua University Press
and Springer-Verlag Berlin
Heidelberg 2017

KEYWORDS

SnS,
sodium ion battery,
anode,
one-step synthesis

ABSTRACT

In this report, we demonstrate a simple chemical bath deposition approach for the synthesis of layered SnS nanosheets (typically 6 nm or ~10 layers thick) at very low temperature (40 °C). We successfully synthesized SnS/C hybrid electrodes using a solution-based carbon precursor coating with subsequent carbonization strategy. Our data showed that the ultrathin carbon shell was critical to the cycling stability of the SnS electrodes. As a result, the as-prepared binder-free SnS/C electrodes showed excellent performance as sodium ion battery anodes. Specifically, the SnS/C anodes delivered a reversible capacity as high as 792 mAh·g⁻¹ after 100 cycles at a current density of 100 mA·g⁻¹. They also had superior rate capability (431 mAh·g⁻¹ at 3,000 mA·g⁻¹) and stable long-term cycling performance under a high current density (345 mAh·g⁻¹ after 500 cycles at 3 A·g⁻¹). Our approach opens up a new route to synthesize SnS-based hybrid materials at low temperatures for energy storage and other applications. Our process will be particularly useful for chalcogenide matrix materials that are sensitive to high temperatures during solution synthesis.

1 Introduction

The ever-increasing demand for large-scale energy storage to support naturally intermittent renewable energy sources has made it imperative that we develop cost-efficient rechargeable batteries [1, 2]. While lithium-ion batteries (LIBs) are widely used in our daily life, the cost and availability of Li are considered serious drawbacks in grid-scale storage applications [3, 4]. Consequently, sodium-ion batteries (SIBs) have been proposed to circumvent these problems due to the low cost, natural abundance, and more suitable

redox potential of Na (E° for Li/Li⁺ = 3.05 V and E° for Na/Na⁺ = 2.71 V vs. SHE at 298 K, 1 M, 1 atm) [5–8]. However, previous studies have demonstrated that most of the potential anodes (including graphite) for Li-ion batteries are ineffective for SIBs [3] because they suffer from low capacity, inferior rate performance, and limited lifespan when used as drop-in replacements in SIBs, which is a serious obstacle to their commercialization. The larger atomic size of sodium ions relative to lithium ions (1.02 Å radius for Na⁺ vs. 0.59 Å radius for Li⁺) is generally thought to be responsible for such a huge performance decay since

Address correspondence to husam.alshareef@kaust.edu.sa

Na diffusion becomes sluggish in the host materials and the hosts undergo a large volume expansion [9, 10]. Hence, there is a strong interest in the development of more suitable SIB anodes. Thus far, tin-based materials (e.g., Sn, SnO_2 , SnO, SnS_2 , and SnS) have been proposed as high-capacity anodes for SIBs, based on the theoretical stoichiometry of $\text{Na}_{3.75}\text{Sn}$ ($847 \text{ mAh}\cdot\text{g}^{-1}$) [11]. However, the large volume expansion of Sn during sodiation ($\sim 420\%$) essentially makes it impossible to achieve such a high theoretical capacity [12]. Therefore, the practical implementation of tin oxides in SIBs has been hindered by their low initial Coulombic efficiency, poor intrinsic conductivity, and inferior cycling stability [13]. For example, Wang et al reported that SnO_2 @graphene electrodes could deliver a reversible capacity of $600 \text{ mAh}\cdot\text{g}^{-1}$ at $20 \text{ mA}\cdot\text{g}^{-1}$, with a very low initial Coulombic efficiency (32%) [14]. Such low Coulombic efficiency probably results from the incomplete transformation of SnO_2 from Sn and Na_2O during the charging process because of the strong Na–O ionic bond [15, 16].

However, tin sulfides offer higher electrical conductivity and weaker metal-sulfur bonds, which make them more appealing for SIBs compared to tin-oxides [13, 16, 17]. Among them, conversion-cum-alloy based SnS_2 and SnS have been the most widely investigated candidates. As shown in Fig. 1(a), hexagonal SnS_2 has a CdI_2 -type sandwich structure that consists of covalently bonded S–Sn–S trilayers with an interlayer distance of 0.59 nm separated by van der Waals forces.

However, orthorhombic SnS shows a different GeS-type layered structure with an interlayer spacing of 0.56 nm compared to SnS_2 (Fig. 1(b)). The ideal interlayer distances of SnS_2 and SnS are suitable for sodium ion insertion and further accommodate the large volume expansion from the Na alloying/de-alloying process. While both SnS_2 and SnS show structural benefits as SIB anodes, we realized that orthorhombic SnS is superior for the following reasons: 1) SnS is reported to have a much narrower band gap (1.11 eV) compared with SnS_2 (2.24 eV) and thus a higher intrinsic conductivity [18], which is desirable for high-rate anodes. 2) As demonstrated earlier, the arrangement of Sn atoms in orthorhombic SnS is similar to that of cubic Sn, which is the phase obtained after sodiation, suggesting that structural instability could be reduced [19]. 3) SnS offers a simpler sodiation-desodiation process, which is beneficial for long-term stability; specifically, the SnS experiences a two-structure phase transformation ($\text{SnS} \rightarrow \alpha\text{-Sn} \rightarrow \text{Na}_{3.75}\text{Sn}$) during the conversion and alloying process, while SnS_2 involves a more complicated reaction mechanism [19, 20]. This difference leads to a substantially larger lattice volume change in the case of SnS_2 (324% for SnS_2 vs. 242% for SnS). 4) SnS shows a comparable high theoretical capacity ($1,022 \text{ mAh}\cdot\text{g}^{-1}$) to SnS_2 ($1,135 \text{ mAh}\cdot\text{g}^{-1}$). Despite these advantages, SnS still exhibits relatively inferior cycling stability from its volume change during Na ion storage (242% from SnS to $\text{Na}_{3.75}\text{Sn}$). To address this issue, carbonaceous materials, such as graphene,

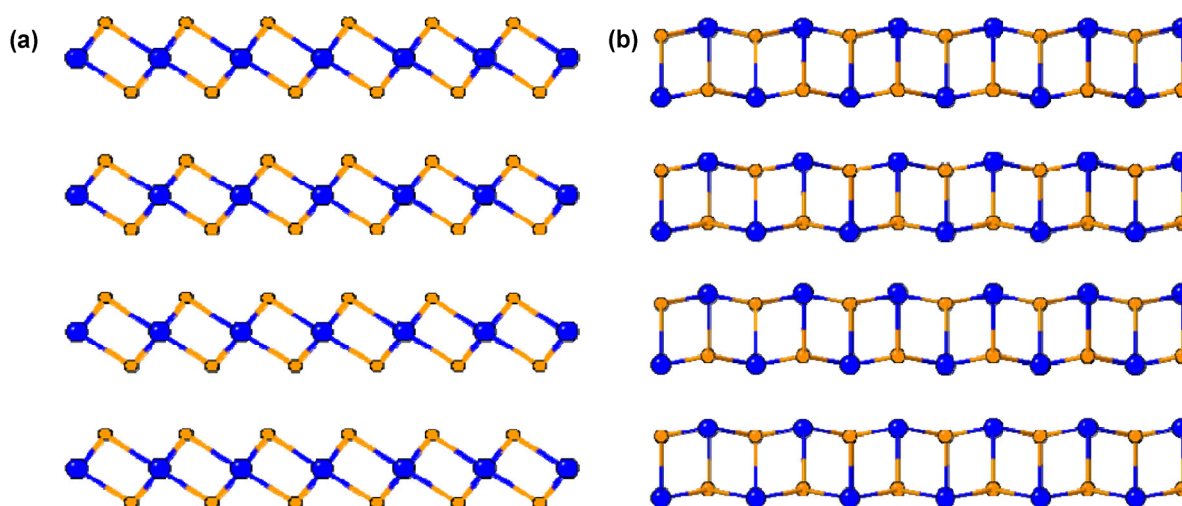


Figure 1 Crystal structures of (a) hexagonal SnS_2 and (b) orthorhombic SnS. Blue atom: Tin; yellow atom: Sulfur.

have been employed to stabilize the sulfide electrodes [16, 21–24]. For instance, Guo et al. showed that SnS/graphene electrodes exhibit a reversible capacity of $940 \text{ mAh}\cdot\text{g}^{-1}$ at $30 \text{ mA}\cdot\text{g}^{-1}$ while pristine SnS exhibits a capacity only around $300 \text{ mAh}\cdot\text{g}^{-1}$ [19]. Furthermore, it has been demonstrated that the pulverization of the electrode materials can be prevented to some degree by reducing their size to the nanoscale [25]. Moreover, ultrathin (or few-layered) 2D materials have been reported to offer higher capacity and better stability than their bulk counterparts [26–28]. Additionally, in the literature, pure SnS and its composite powders have been used for SIB tests with binders (e.g., PVDF), which have recently been found to accelerate the deterioration of the electrodes during sodiation [29]. Therefore, binder-free electrodes are clearly more suitable for high-performance battery applications.

To date, the structural phase transition method (conversion of SnS_2 to SnS via 550°C Ar annealing) has been the most commonly used approach to synthesize SnS, which is impractical due to its high cost and multiple steps. In addition, our research shows that the direct conversion of SnS_2 nanosheets (a desirable morphology for SIB anodes) to SnS using high temperature annealing is virtually impossible without significantly changing the nanosheet morphology, which will be discussed later in the manuscript. Thus, an alternative to the phase transition method is needed to convert SnS_2 to SnS without destroying the nanosheet morphology. Herein, we present a one-step solution process to realize the fast growth of ultrathin SnS nanosheets on highly conductive carbon fiber paper (CFP) near room temperature (40°C , 2 h). Then, we successfully synthesized the SnS/C hybrid electrodes for SIBs using a solution-based carbon precursor coating and subsequent carbonization strategy. The synthesized SnS/C electrodes exhibited a high reversible capacity of $791 \text{ mAh}\cdot\text{g}^{-1}$ at $100 \text{ mA}\cdot\text{g}^{-1}$ after 100 cycles and, impressively, $431 \text{ mAh}\cdot\text{g}^{-1}$ after a 30-fold increase in current density to $3 \text{ A}\cdot\text{g}^{-1}$.

2 Experimental

2.1 Synthesis of orthorhombic SnS

The SnS nanoarrays were synthesized using a chemical

bath deposition process. Typically, $0.05 \text{ mol SnCl}_2\cdot 2\text{H}_2\text{O}$ and 0.15 mol thioacetamide were dissolved in 240 mL N_2 saturated ethanol in a glass bottle followed by 2 min sonication to yield a clear solution. Then, a piece of carbon fiber paper (CFP) was immersed into the above solution. The deposition was then carried out at 40°C for 2 h. Immediately, the transparent solution became opaque and brown. After cooling down to the room temperature ($20\text{--}25^\circ\text{C}$), the obtained free-standing SnS powder and SnS nanosheets on CFP were washed with deionized water and ethanol. Finally, all the samples were dried in vacuum at 60°C . For the SnS_2 synthesis, 0.05 mol SnCl_4 was used to replace SnCl_2 . In that case, the temperature and chemical bath deposition reaction time were increased to 60°C and 4 h, respectively.

2.2 Synthesis of orthorhombic SnS/Carbon on CFP

In a typical procedure, one piece of the as-prepared SnS/CFP was soaked in 80 mL of a 0.1 M glucose aqueous solution under ambient conditions for 6 h. Then, the CFP was dried at room temperature without washing. Next, the SnS/glucose/CFP sample was annealed at 550°C under an Ar atmosphere for 1 h to prepare the final products (SnS/Carbon on CFP).

2.3 Synthesis of SnS/ SnO_2 /Carbon on CFP

In a typical procedure, one piece of the as-prepared SnS/CFP was immersed in 40 mL of a 0.1 M glucose aqueous solution for 10 min. Then, this solution was subsequently transferred into a Teflon-lined autoclave with CFP and held at 180°C for 3 h. After cooling down to room temperature, the CFP was collected and washed with deionized water and ethanol. The CFP was dried in vacuum at 60°C .

2.4 Synthesis of SnS nanoparticle on CFP

In a typical procedure, one piece of the as-prepared SnS_2 /CFP was annealed at 550°C under an Ar atmosphere for 1 h.

2.5 Structural characterization

X-ray diffraction (XRD) patterns were collected by a Bruker diffractometer (D8 Advance) with $\text{Cu K}\alpha$ radiation with $\lambda = 1.5406 \text{ \AA}$. X-ray photoelectron

spectroscopy (XPS) analysis was conducted using a Kratos AXIS Ultra DLD spectrometer. The morphology and microstructure of the samples were characterized by scanning electron microscopy (SEM, Nova Nano 630, FEI) and transmission electron microscopy (TEM, Titan 80–300 kV). Atomic force microscopy (AFM) images were recorded using a Digital Instrument Multi-Mode AFM with a Nanoscope 4 controller operating in tapping mode. Raman spectra were collected using a Hariba LabRAM HR spectrometer.

2.6 Electrochemical measurements

For electrochemical measurements, SnS/CFP and SnS/Carbon/CFP were directly used as binder-free working electrodes. The CR2032-type coin half-cells, using sodium foil as the counter electrode, were assembled in an argon-filled glove box, where both H₂O and O₂ concentrations were less than 1 ppm. The separator was a Celgard 3501 microporous membrane, and the electrolyte was a 1 M solution of NaClO₄ dissolved in ethylene carbonate/DMC with a 1:1 weight ratio. Cyclic voltammetry was performed by a Biologic VMP3 electrochemistry workstation in the voltage range of 0.01–2.0 V (vs. Na/Na⁺) at a scan rate of 0.1 mV·s⁻¹. The galvanostatic discharge-charge cycles at different current density states were performed by an Arbin BT-2043 battery testing system in the voltage range of 0.01–2.0 V.

3 Results and discussion

The growth of a large area of well-aligned SnS nanosheets was realized using a chemical bath deposition process by reacting SnCl₂·2H₂O and thioacetamide in anhydrous ethanol at 40 °C for 2 h. The reactions involved in the formation of ultrathin SnS nanosheets can be described as follows [30]

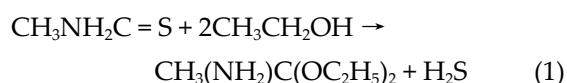


Figure S1 in the Electronic Supplementary Material (ESM) shows a digital photo of tin sulfide powder that was prepared using our chemical bath deposition

method. Clearly, these powders have a dark brown color, which differs from the yellow SnS₂, implying the formation of SnS instead of SnS₂. The crystal structure of the as-prepared tin sulfide on CFP was characterized using XRD. The black curve in Fig. 2(a) reveals the θ -2 θ XRD pattern of the near-room temperature synthesized tin sulfide. Clearly, all the diffraction peaks matched with orthorhombic SnS (JCPDS No. 39-0354) without any detectable impurity phases. Furthermore, the sharp peaks also indicate the high crystallinity of our samples despite the low temperature synthesis. Raman spectroscopy was also used to further characterize our SnS nanosheets. As shown in Fig. 2(b), four distinguishable peaks were observed. The peaks centered at 60 and 312 cm⁻¹ originated from the second order multiple phonon scattering process of orthorhombic SnS, whereas the peaks located at 93 and 223 cm⁻¹ belonged to the first order single phonon oriented transverse or longitudinal optical vibrational modes of SnS [31, 32]. The Raman analysis further demonstrated the formation of highly pure orthorhombic SnS. We then performed XPS measurements where the high-resolution Sn 3d and S 2p spectra are displayed in Figs. 2(c) and 2(d). The peak at 486.3 eV in Fig. 2(c) corresponded to the Sn 3d_{5/2} of Sn²⁺ [33]. Obviously, Sn⁴⁺ was not detected in the spectrum. In addition, the peaks at 161.3 and 162.6 eV in Fig. 2(d) could be assigned to S 2p_{3/2} and S 2p_{1/2} in an S²⁻-like chemical state, respectively, with binding energy that is very close to the reported single crystal SnS nanowires [34]. Moreover, unlike previous reports [19], no thiol groups were observed in the S 2p spectrum. Thus, the XPS results also confirmed the formation of high purity crystalline SnS products. We also tried to prepare SnS nanosheets by the reported structural phase transformation method using the SnS₂ nanosheet array as the template. As shown in Fig. S2 in the ESM, the original morphology of the SnS₂ nanosheets was completely destroyed after 1 h of annealing in Ar at 550 °C. In this case, the ultrathin SnS₂ nanosheets aggregated into large particles and were subsequently reduced to SnS (Fig. S2(c) in the ESM). This result further demonstrates the advantage of our low-temperature synthesis route.

The morphology and microstructure of the as-prepared SnS on CFP were examined using SEM

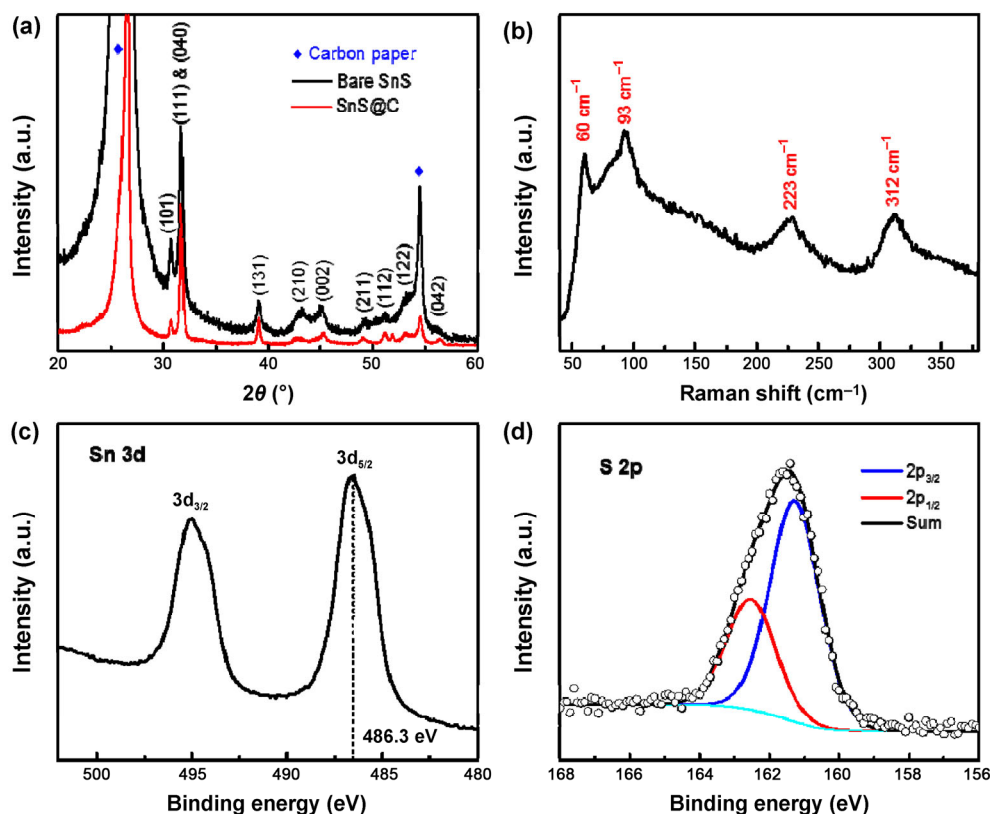


Figure 2 (a) Representative XRD patterns for the as-prepared bare SnS and SnS/C nanosheets on CFP. (b) Raman spectrum of the fresh SnS/CFP anode. High-resolution XPS spectra of (c) Sn 3d and (d) S 2p of pristine SnS.

and TEM. As shown in Figs. 3(a) and (b), the CFP substrate was uniformly covered with vertically aligned SnS nanosheets. The abundant open pores between the interconnected SnS nanosheets are believed to boost the electrolyte ion trapping and improve its access to the active materials. The TEM image (Fig. 3(c)) provides more detail about the properties of the SnS ultrathin nanosheets with a lateral sheet size of around 1 μm . The lattice fringe in the high-resolution TEM (HRTEM) image (Fig. 3(d)) was determined to be 2.82 \AA , corresponding to the (111) planes of orthorhombic SnS. As shown in Fig. S3 in the ESM, AFM analysis indicated that the SnS nanosheets are typically 6 nm thick (~ 10 layers), confirming their ultrathin 2D character. The diffusion time of alkali metal ions in electrode materials is well known to be proportional to the square of the diffusion length; thus, the ultrathin nature of these SnS sheets could be expected to lead to faster ion diffusion and better rate performance of our SnS anodes [19, 35]. Furthermore, as mentioned earlier, the reduced thickness of 2D materials can

enhance cycling stability in battery applications [36–38]. A common approach used to protect the electrode from direct contact with the electrolyte in batteries is a surface coating, which often leads to improved cycling stability of anodes [39]. Here, we also expected that the cycling performance of our SnS phase could be further enhanced by carbon coating. Our experimental results showed that the deposition of a carbon layer via the commonly used glucose-hydrothermal-decomposition-process did not work well for our SnS anodes. To be specific, as shown in Fig. S4 in the ESM, the SEM and XRD data indicate that after the glucose hydrothermal decomposition reaction, the SnS nanosheets were partially oxidized into SnO_2 . Thus, another approach was needed that preserved the composition and structure of the SnS phase. A solution-based carbon precursor coating and subsequent carbonization strategy was employed to form such a thin protective carbon layer on the surface of SnS [40]. In this process, the SnS/CFP electrode was soaked in a glucose aqueous solution, dried at

ambient conditions without washing, and then annealed at 550 °C in an Ar atmosphere. During the annealing process, the surface adsorbed glucose dehydrated the cross-link, followed by aromatization and carbonization, resulting in a firm carbonized shell covering the SnS anode surfaces [40, 41]. The θ - 2θ XRD pattern of SnS/C (red curve in Fig. 2(a)) clearly shows that no structural changes occurred during the formation of the protective carbon layer and that the SnS structure and composition remained intact. Figures 3(e) and 3(f) demonstrate that the SnS/C nanostructures retained the original morphology of pure SnS, but the surface had roughened. In addition, the TEM analysis (Figs. 3(g) and 3(h)) clearly reveals that the SnS nanosheets had become uniformly surrounded by a carbon shell with a thickness of a few nanometers (4–6 nm). The selected area electron diffraction (SAED)

image (Fig. 3(i)) demonstrates the single crystalline (clear diffraction spots) and partially graphitic (two diffuse rings) nature of SnS and carbon in SnS/C, respectively.

To investigate the anode performance of the as-prepared SnS/C electrodes for SIBs, cyclic voltammetry (CV) measurements were performed. Figure 4(a) displays the initial three CV curves of SnS/C anodes at a scan rate of 0.1 mV·s⁻¹ in the voltage range of 0.01–2.0 V. During the 1st cathodic sweep, a distinct peak centered at 0.72 V was observed. This peak could be ascribed to the conversion of SnS to Sn metal nanograins and amorphous Na₂S, subsequent alloying reactions of Sn, and the decomposition of the electrolyte to form a solid-electrolyte interphase (SEI) layer [5, 16, 19, 23]. After the 1st CV scan, this peak splits into two peaks at around 1.1 and 0.6 V, which represent

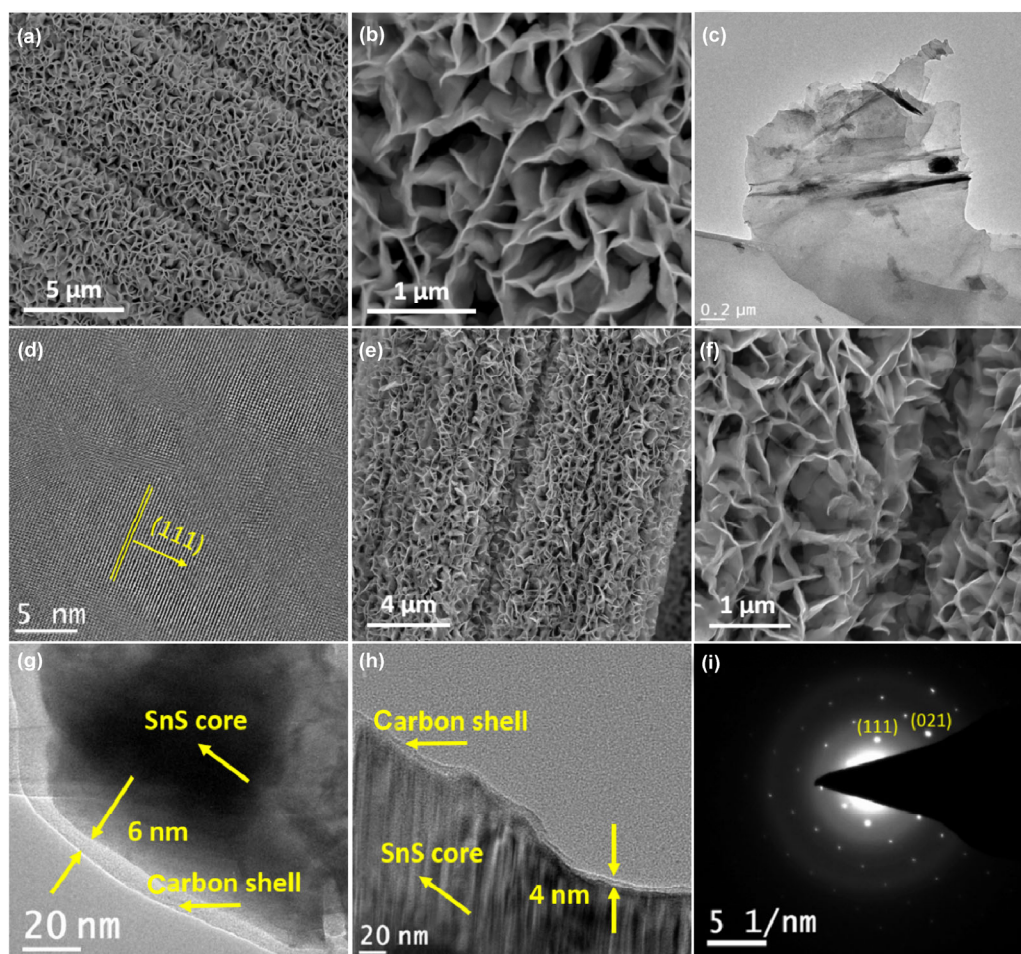


Figure 3 (a) and (b) Representative SEM images of the as-prepared pure SnS on CFP showing the well-defined nanosheet architecture. (c) and (d) The TEM images for individual SnS nanosheets. Typical (e) and (f) SEM and (g) and (h) TEM images of the SnS/C core-shell hybrid structure. (i) A representative SAED pattern for individual SnS/C nanosheets.

the conversion reaction of SnS and alloying process of Sn, respectively. It is generally accepted that the alloying reaction between Sn and Na is a multistep process [12]. First, NaSn_4 forms at around 0.7 V. Then, with decreasing potential, more Na ions are incorporated into NaSn_4 to form Na_xSn ($x \leq 3.75$). Thus, the broad reduction peak below 0.7 V was attributed to the additional formation of Na–Sn alloys. During the 1st anodic scan, the oxidation peaks at 0.29 and 0.71 V could be assigned to the multistep dealloying process of Na_xSn to Sn. The oxidation peaks at 1.09 and 1.34 V could be ascribed to the restitution of SnS (from Sn to

SnS). As shown in Fig. 4(a), the CV curves had no obvious area loss, implying the stability of the SnS/C electrodes. We further performed a deep galvanostatic charge-discharge (CD) scan between 0.01 and 2.0 V to further investigate the SnS/C electrode performance in SIBs. On deep galvanostatic cycling (Fig. 4(b)), the discharge capacity was 1,252 $\text{mAh}\cdot\text{g}^{-1}$, and the charge capacity was 928 $\text{mAh}\cdot\text{g}^{-1}$ in the first cycle at a current density of 100 $\text{mA}\cdot\text{g}^{-1}$, which corresponds to an initial Coulombic efficiency of ~74%. On the 5th cycle, the Coulombic efficiency of SnS/C increases up to ~99%. The irreversible capacity of the 1st CD scan was

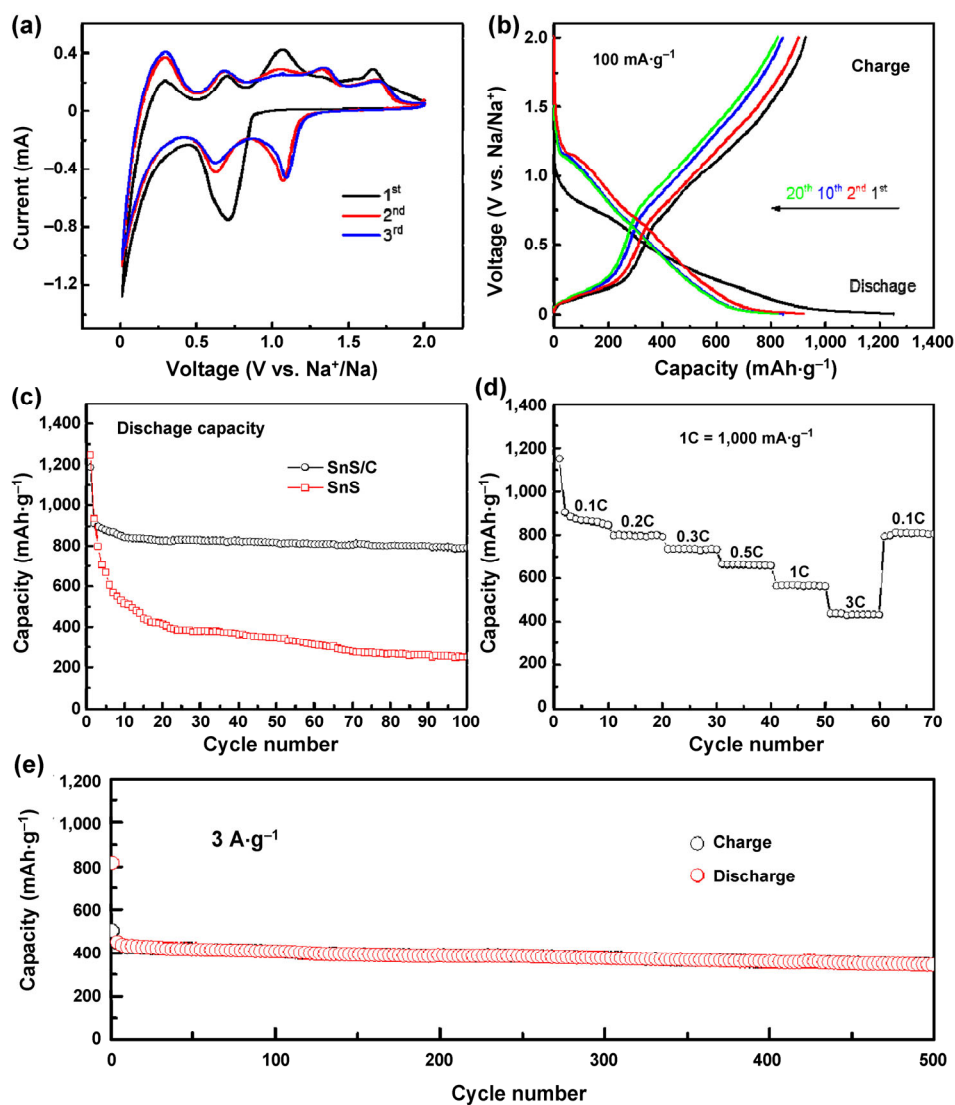


Figure 4 (a) Cyclic voltammograms for the first three cycles of the SnS/C electrode at a scan rate of 0.1 $\text{mV}\cdot\text{s}^{-1}$. (b) Galvanostatic charge-discharge plots of the SnS/C electrode at the 1st, 2nd, 10th, and 20th cycles. (c) Cycling performance of the SnS and SnS/C electrode at 100 $\text{mA}\cdot\text{g}^{-1}$ for 100 cycles. (d) Rate performance of SnS/C hybrid electrode. (e) Long-term cycling performance of the SnS/C nanosheet at a current density of 3,000 $\text{mA}\cdot\text{g}^{-1}$.

mainly due to the consumption of Na ions during SEI layer formation, which is consistent with the CV tests. Furthermore, the charge/discharge voltage plateaus were notably consistent with the CV results. As shown in Fig. 4(c), the SnS/C electrodes show good cycling stability from the 2nd cycle onwards, whereas the cycling stability of pure SnS is very poor. Specifically, SnS/C electrode delivered discharge capacities of 913, 818, 792 mAh·g⁻¹ in the 2nd, 50th, and 100th cycles, respectively, demonstrating an 87% capacity retention after 100 cycles. However, the pristine SnS electrodes suffered from dramatic capacity decay, retaining only 33% of the second cycle capacity after 20 CD cycles. Such poor cycling stability validated our argument that the SnS/C hybrid electrode is a more suitable choice than bare SnS for SIBs because the thin carbon layer buffered the large volume change. Furthermore, the carbon layer served as the “glue” to integrate the nanosized particles during the sodiation and desodiation processes to avoid the complete pulverization of each individual SnS nanosheet. Notably, the reversible capacity of the SnS/C reported here was higher than the values reported so far for SnS₂-based hybrid SIB electrodes, such as SnS₂/C (660 mAh·g⁻¹ at 50 mA·g⁻¹) [42], SnS₂/rGO (671 mAh·g⁻¹ at 100 mA·g⁻¹) [43], few-layered SnS₂/rGO (649 mAh·g⁻¹ at 100 mA·g⁻¹) [44], and exfoliated SnS₂/graphene (650 mAh·g⁻¹ at 200 mA·g⁻¹) [24]. The superior SIB performance of the SnS/C electrode also verified our above argument that SnS is a more suitable anode candidate than SnS₂. In addition, the plot of Coulombic efficiency vs. cycle number proves the high reversibility and high efficiency of this SnS/C electrode (Fig. S5 in the ESM).

As an important performance indicator for grid-scale electricity storage, the rate performance of the SnS/C electrodes was investigated. The good rate capability of SnS/C is illustrated in Fig. 4(d), where the current density was increased step-wise from 0.1 to 3 A·g⁻¹ and returned to 0.1 A·g⁻¹. Note that ten cycles were used for each step. The 10th discharge capacities at 0.1, 0.2, 0.3, 0.5, 1, and 3 A·g⁻¹ were 843, 792, 734, 662, 562, and 431 mAh·g⁻¹, respectively. Impressively, a high discharge capacity could be achieved at 3 A·g⁻¹, which represents a 30-fold increase in current density corresponding to ~52% of the discharge capacity at 0.1 A·g⁻¹. In addition, when the

current density was returned to 0.1 A·g⁻¹, the discharge capacity recovered to 806 mAh·g⁻¹, suggesting that the SnS/C anodes can tolerate high-rate cycling without anode degradation [44, 45]. These results demonstrate that the binder-free SnS/C nanosheets with free electrical transport pathways and large volume separation ratios could allow high-speed Na ion transformation without irreversible changes. We also examined their long-term cycling stability at a high current density of 3 A·g⁻¹. As shown in Fig. 4(e), the SnS/C anode still shows a reversible capacity of 345 mAh·g⁻¹ after 500 cycles, demonstrating the excellent cycling stability of these SnS/C anode nanosheets. The SIB performance of our SnS/C electrode was outstanding compared to previously reported SIB anodes including carbonaceous material, metal alloy, metal oxides/sulfides/carbides as shown in Table S1. This result combined with the simple synthesis process near room temperature shows that SnS/C is indeed a very promising anode material for SIBs.

4 Conclusions

In summary, we have developed layered SnS anodes for Na ion batteries using a simple chemical bath deposition approach at very low temperature. The optimized anodes were subsequently coated with a carbon surface layer using a solution-based carbon precursor coating and carbonization strategy. As a result, the as-prepared binder-free SnS/C electrodes showed excellent performance as SIB anodes. Specifically, the SnS/C anodes delivered a reversible capacity as high as 792 mAh·g⁻¹ after 100 cycles at a current density of 100 mA·g⁻¹. They also showed superior rate capability (431 mAh·g⁻¹ at 3,000 mA·g⁻¹) and stable long-term cycling performance under high current density (345 mAh·g⁻¹ after 500 cycles at 3 A·g⁻¹). Our approach opens up a new route to synthesize SnS-based hybrid materials at low temperatures, which is particularly useful for chalcogenide matrix materials that are sensitive to high temperatures during solution synthesis.

Acknowledgements

Research reported in this publication has been

supported by King Abdullah University of Science and Technology (KAUST). The authors wish to thank Mr. Zhenwei Wang for his help with the AFM analysis.

Electronic Supplementary Material: Supplementary material (digital photos of SnS_2 and SnS , further characterizations, AFM of SnS nanosheet) is available in the online version of this article at: <https://doi.org/10.1007/s12274-017-1722-0>.

References

- [1] Wang, Q.; Wang, C. Y.; Zhang, M. C.; Jian, M. Q.; Zhang, Y. Y. Feeding single-walled carbon nanotubes or graphene to silkworms for reinforced silk fibers. *Nano Lett.* **2016**, *16*, 6695–6700.
- [2] Chen, Y. N.; Luo, W.; Carter, M.; Zhou, L. H.; Dai, J. Q.; Fu, K.; Lacey, S.; Li, T.; Wan, J. Y.; Han, X. G. et al. Organic electrode for non-aqueous potassium-ion batteries. *Nano Energy* **2015**, *18*, 205–211.
- [3] Kim, S. W.; Seo, D. H.; Ma, X. H.; Ceder, G.; Kang, K. Electrode materials for rechargeable sodium-ion batteries: Potential alternatives to current lithium-ion batteries. *Adv. Energy Mater.* **2012**, *2*, 710–721.
- [4] Yabuuchi, N.; Kubota, K.; Dahbi, M.; Komaba, S. Research development on sodium-ion batteries. *Chem. Rev.* **2014**, *114*, 11636–11682.
- [5] Dutta, P. K.; Sen, U. K.; Mitra, S. Excellent electrochemical performance of tin monosulphide (SnS) as a sodium-ion battery anode. *RSC Adv.* **2014**, *4*, 43155–43159.
- [6] Pan, H. L.; Hu, Y. S.; Chen, L. Q. Room-temperature stationary sodium-ion batteries for large-scale electric energy storage. *Energy Environ. Sci.* **2013**, *6*, 2338–2360.
- [7] Peng, L. L.; Zhu, Y.; Chen, D. H.; Ruoff, R. S.; Yu, G. H. Two-dimensional materials for beyond-lithium-ion batteries. *Adv. Energy Mater.* **2016**, *6*, 1600025.
- [8] Li, H. S.; Zhu, Y.; Dong, S. Y.; Shen, L. F.; Chen, Z. J.; Zhang, X. G.; Yu, G. H. Self-assembled Nb_2O_5 nanosheets for high energy-high power sodium ion capacitors. *Chem. Mater.* **2016**, *28*, 5753–5760.
- [9] Park, Y. U.; Seo, D. H.; Kwon, H. S.; Kim, B.; Kim, J.; Kim, H.; Kim, I.; Yoo, H. I.; Kang, K. A new high-energy cathode for a Na-ion battery with ultrahigh stability. *J. Am. Chem. Soc.* **2013**, *135*, 13870–13878.
- [10] Li, H. S.; Peng, L. L.; Zhu, Y.; Chen, D. H.; Zhang, X. G.; Yu, G. H. An advanced high-energy sodium ion full battery based on nanostructured $\text{Na}_2\text{Ti}_3\text{O}_7/\text{VOPO}_4$ layered materials. *Energy Environ. Sci.* **2016**, *9*, 3399–3405.
- [11] Li, Z.; Ding, J.; Mitlin, D. Tin and tin compounds for sodium ion battery anodes: Phase transformations and performance. *Acc. Chem. Res.* **2015**, *48*, 1657–1665.
- [12] Wang, J. W.; Liu, X. H.; Mao, S. X.; Huang, J. Y. Microstructural evolution of tin nanoparticles during *in situ* sodium insertion and extraction. *Nano Lett.* **2012**, *12*, 5897–5902.
- [13] Zheng, Y.; Zhou, T. F.; Zhang, C. F.; Mao, J. F.; Liu, H. K.; Guo, Z. P. Boosted charge transfer in SnS/SnO_2 heterostructures: Toward high rate capability for sodium-ion batteries. *Angew. Chem., Int. Ed.* **2016**, *55*, 3408–3413.
- [14] Su, D. W.; Ahn, H. J.; Wang, G. X. $\text{SnO}_2@$ graphene nanocomposites as anode materials for Na-ion batteries with superior electrochemical performance. *Chem. Commun.* **2013**, *49*, 3131–3133.
- [15] Hildenbrand, D. L.; Murad, E. Dissociation energy of NaO(g) and the heat of atomization of $\text{Na}_2\text{O(g)}$. *J. Chem. Phys.* **1970**, *53*, 3403–3408.
- [16] Wu, L.; Lu, H. Y.; Xiao, L. F.; Qian, J. F.; Ai, X. P.; Yang, H. X.; Cao, Y. L. A tin(II) sulfide-carbon anode material based on combined conversion and alloying reactions for sodium-ion batteries. *J. Mater. Chem. A* **2014**, *2*, 16424–16428.
- [17] Zhu, C. B.; Kopold, P.; Li, W. H.; van Aken, P. A.; Maier, J.; Yu, Y. A general strategy to fabricate carbon-coated 3D porous interconnected metal sulfides: Case study of SnS/C nanocomposite for high-performance lithium and sodium ion batteries. *Adv. Sci.* **2015**, *2*, 1500200.
- [18] Burton, L. A.; Colombara, D.; Abellon, R. D.; Grozema, F. C.; Peter, L. M.; Savenije, T. J.; Dennler, G.; Walsh, A. Synthesis, characterization, and electronic structure of single-crystal SnS , Sn_2S_3 , and SnS_2 . *Chem. Mater.* **2013**, *25*, 4908–4916.
- [19] Zhou, T. F.; Pang, W. K.; Zhang, C. F.; Yang, J. P.; Chen, Z. X.; Liu, H. K.; Guo, Z. P. Enhanced sodium-ion battery performance by structural phase transition from two-dimensional hexagonal- SnS_2 to orthorhombic- SnS . *ACS Nano* **2014**, *8*, 8323–8333.
- [20] Im, H. S.; Cho, Y. J.; Lim, Y. R.; Jung, C. S.; Jang, D. M.; Park, J.; Shojaei, F.; Kang, H. S. Phase evolution of tin nanocrystals in lithium ion batteries. *ACS Nano* **2013**, *7*, 11103–11111.
- [21] Xin, S.; Guo, Y. G.; Wan, L. J. Nanocarbon networks for advanced rechargeable lithium batteries. *Acc. Chem. Res.* **2012**, *45*, 1759–1769.
- [22] Xie, X. Q.; Su, D. W.; Chen, S. Q.; Zhang, J. Q.; Dou, S. X.; Wang, G. X. SnS_2 nanoplatelet@ graphene nanocomposites as high-capacity anode materials for sodium-ion batteries. *Chem.-Asian J.* **2014**, *9*, 1611–1617.
- [23] Choi, S. H.; Kang, Y. C. Aerosol-assisted rapid synthesis of $\text{SnS}-\text{C}$ composite microspheres as anode material for Na-ion batteries. *Nano Res.* **2015**, *8*, 1595–1603.

- [24] Liu, Y. C.; Kang, H. Y.; Jiao, L. F.; Chen, C. C.; Cao, K. Z.; Wang, Y. J.; Yuan, H. T. Exfoliated-SnS₂ restacked on graphene as a high-capacity, high-rate, and long-cycle life anode for sodium ion batteries. *Nanoscale* **2015**, *7*, 1325–1332.
- [25] Liu, S.; Yin, X. M.; Hao, Q. Y.; Zhang, M.; Li, L. M.; Chen, L. B.; Li, Q. H.; Wang, Y. G.; Wang, T. H. Chemical bath deposition of SnS₂ nanowall arrays with improved electrochemical performance for lithium ion battery. *Mater. Lett.* **2010**, *64*, 2350–2353.
- [26] Bang, G. S.; Nam, K. W.; Kim, J. Y.; Shin, J.; Choi, J. W.; Choi, S. Y. Effective liquid-phase exfoliation and sodium ion battery application of MoS₂ nanosheets. *ACS Appl. Mater. Interfaces* **2014**, *6*, 7084–7089.
- [27] Chen, L.; Zhou, G. M.; Liu, Z. B.; Ma, X. M.; Chen, J.; Zhang, Z. Y.; Ma, X. L.; Li, F.; Cheng, H. M.; Ren, W. C. Scalable clean exfoliation of high-quality few-layer black phosphorus for a flexible lithium ion battery. *Adv. Mater.* **2016**, *28*, 510–517.
- [28] Wang, Q.; Pan, J.; Li, M.; Luo, Y. Y.; Wu, H.; Zhong, L.; Li, G. H. VO₂ (B) nanosheets as a cathode material for Li-ion battery. *J. Mater. Sci. Technol.* **2015**, *31*, 630–633.
- [29] Chao, D. L.; Liang, P.; Chen, Z.; Bai, L. Y.; Shen, H.; Liu, X. X.; Xia, X. H.; Zhao, Y. L.; Savilov, S. V.; Lin, J. Y. et al. Pseudocapacitive Na-ion storage boosts high rate and areal capacity of self-branched 2D layered metal chalcogenide nanoarrays. *ACS Nano* **2016**, *10*, 10211–10219.
- [30] Yang, W. L.; Zhang, L.; Hu, Y.; Zhong, Y. J.; Wu, H. B.; Lou, X. W. D. Microwave-assisted synthesis of porous Ag₂S–Ag hybrid nanotubes with high visible-light photocatalytic activity. *Angew. Chem., Int. Ed.* **2012**, *51*, 11501–11504.
- [31] Reddy, N. K. Growth-temperature dependent physical properties of SnS nanocrystalline thin films. *ECS J. Solid State Sci. Technol.* **2013**, *2*, P259–P263.
- [32] Devika, M.; Reddy, N. K.; Prashantha, M.; Ramesh, K.; Reddy, S. V.; Hahn, Y. B.; Gunasekhar, K. R. The physical properties of SnS films grown on lattice-matched and amorphous substrates. *Phys. Status Solidi (A)* **2010**, *207*, 1864–1869.
- [33] Alam, F.; Dutta, V. Tin sulfide (SnS) nanostructured films deposited by continuous spray pyrolysis (CoSP) technique for dye-sensitized solar cells applications. *Appl. Surf. Sci.* **2015**, *358*, 491–497.
- [34] Yue, G. H.; Lin, Y. D.; Wen, X.; Wang, L. S.; Chen, Y. Z.; Peng, D. L. Synthesis and characterization of the SnS nanowires via chemical vapor deposition. *Appl. Phys. A* **2012**, *106*, 87–91.
- [35] Aricò, A. S.; Bruce, P.; Scrosati, B.; Tarascon, J. M.; Van Schalkwijk, W. Nanostructured materials for advanced energy conversion and storage devices. *Nat. Mater.* **2005**, *4*, 366–377.
- [36] Rangappa, D.; Murukanahally, K. D.; Tomai, T.; Unemoto, A.; Honma, I. Ultrathin nanosheets of Li₂MSiO₄ (M = Fe, Mn) as high-capacity Li-ion battery electrode. *Nano Lett.* **2012**, *12*, 1146–1151.
- [37] Zhang, K.; Kim, H. J.; Shi, X. J.; Lee, J. T.; Choi, J. M.; Song, M. S.; Park, J. H. Graphene/acid coassisted synthesis of ultrathin MoS₂ nanosheets with outstanding rate capability for a lithium battery anode. *Inorg. Chem.* **2013**, *52*, 9807–9812.
- [38] Ryu, J.; Hong, D. K.; Choi, S.; Park, S. Synthesis of ultrathin Si nanosheets from natural clays for lithium-ion battery anodes. *ACS Nano* **2016**, *10*, 2843–2851.
- [39] Li, H. Q.; Zhou, H. S. Enhancing the performances of Li-ion batteries by carbon-coating: Present and future. *Chem. Commun.* **2012**, *48*, 1201–1217.
- [40] Zhang, Z. H.; Dua, R.; Zhang, L. B.; Zhu, H. B.; Zhang, H. N.; Wang, P. Carbon-layer-protected cuprous oxide nanowire arrays for efficient water reduction. *ACS Nano* **2013**, *7*, 1709–1717.
- [41] Li, Z. Q.; Guo, H. C.; Qian, H. S.; Hu, Y. Facile microemulsion route to coat carbonized glucose on upconversion nanocrystals as high luminescence and biocompatible cell-imaging probes. *Nanotechnology* **2010**, *21*, 315105.
- [42] Wang, J. J.; Luo, C.; Mao, J. F.; Zhu, Y. J.; Fan, X. L.; Gao, T.; Mignerey, A. C.; Wang, C. S. Solid-state fabrication of SnS₂/C nanospheres for high-performance sodium ion battery anode. *ACS Appl. Mater. Interfaces* **2015**, *7*, 11476–11481.
- [43] Qu, B. H.; Ma, C. Z.; Ji, G.; Xu, C. H.; Xu, J.; Meng, Y. S.; Wang, T. H.; Lee, J. Y. Layered SnS₂-reduced graphene oxide composite—a high-capacity, high-rate, and long-cycle life sodium-ion battery anode material. *Adv. Mater.* **2014**, *26*, 3854–3859.
- [44] Zhang, Y. D.; Zhu, P. Y.; Huang, L. L.; Xie, J.; Zhang, S. C.; Cao, G. S.; Zhao, X. B. Few-layered SnS₂ on few-layered reduced graphene oxide as na-ion battery anode with ultralong cycle life and superior rate capability. *Adv. Funct. Mater.* **2015**, *25*, 481–489.
- [45] Zhou, N. J.; Lin, H.; Lou, S. J.; Yu, X. G.; Guo, P. J.; Manley, E. F.; Loser, S.; Hartnett, P.; Huang, H.; Wasielewski, M. R. et al. Morphology-performance relationships in high-efficiency all-polymer solar cells. *Adv. Energy Mater.* **2014**, *4*, 130078.